concerning the hypothesis of the 100-kyr cyclicity in the input of interplanetary dust, will probably be provided by measuring the concentrations of platinum group elements in Antarctic ice records such as those obtained at Dome C and Vostok, as these are relatively less affected by the input of terrestrial dust. □

Methods

Polar ice cores have provided valuable historical records of changes in heavy-metal fluxes in the Earth's atmosphere[23,24]. Until now, the Ir occurrence in polar ice sheets was thought to be related mainly to the deposition of micrometeorites—extraterrestrial particles smaller than ~1 mm in diameter that do not ablate in the mesosphere. The few attempts to measure ultralow levels of Ir in ice cores have been restricted to particles larger than 0.45 μm, obtained from filtered samples[13]. Unfortunately, it has been shown that the typically small volumes retrieved from ice cores caused a severe under-sampling of the micrometeorite input[25]. Statistically significant collections of micrometeorites have required large masses, of up to 8,000 t, of polar ice and firn to be investigated[26].

In contrast with the situation for micrometeorites, ice cores can be used to estimate the input of meteoroids that do not survive entry into the Earth's atmosphere (estimated to lie between 60% and nearly 100% of the total)[16]. Because of their very high entry velocities, meteoroids undergo rapid frictional heating by collision with atmospheric molecules. Their constituent minerals subsequently vaporize between an altitude of 80 and 120 km (refs 5, 6). In the middle mesosphere (50–80 km), the resulting metallic compounds are believed to polymerize with silicon oxides to form metal-rich nanoparticles known as meteoric smoke[5].

As a consequence, platinum-group elements (PGEs), which are highly enriched in chondritic meteorites[12], are redistributed from individual submillimetric particles onto multiple nanometric particles before deposition at the Earth's surface. Thus, the concentration of PGEs in ice cores can be used to evaluate the ablated fraction of the meteoroid input. Furthermore, ice cores benefit from three relevant advantages with respect to other environmental archives for studying PGEs on a long timescale. First, the properties of PGEs remain unaltered in a low interference matrix such as ice; second, their deposition can be dated more precisely; and last, their flux can be calculated via the better known past accumulation rate.

Traditional methods for determining Ir in micrometric particulate matter filtered from ice samples[13] fail to include the potentially significant contribution from the much smaller sized meteoric smoke. This can only be taken into account by measuring the total Ir concentration relative to the wet mass of the sample. Recently, on the basis of experience in measuring PGEs in ice cores by using inductively coupled plasma sector field mass spectrometry (ICP-SFMS)[27], we have developed a new method (see details in ref. 14) for quantifying the total concentration of Ir and Pt in ice, down to the sub-fg g^{-1} level. Ultra-clean procedures and a preconcentration step have enabled us to achieve negligible procedural blanks (see also Supplementary Method 1) and procedural detection limits of 0.02 and 0.08 fg g^{-1} for Ir and Pt, respectively[14]. This method benefits from an ultra-clean chemical processing of the sample based on the simple addition of ultrapure HNO_3 to the melted and pre-concentrated ice samples. The complete ionization of the meteoric smoke in the plasma (at ~7,000 K) of the ICP-SFMS is assured by the already quasi-molecular size of these particles, without the need to add any supplemental chemical reagent.

Received 20 May; accepted 18 October 2004; doi:10.1038/nature03137.

1. Alvarez, L. W., Alvarez, W., Asaro, F. & Michel, H. V. Extraterrestrial cause for the Cretaceous/Tertiary extinction. *Science* **208,** 1095–1108 (1980).
2. Schuraytz, B. C. *et al.* Iridium metal in Chicxulub impact melt: forensic chemistry on the K-T smoking gun. *Science* **271,** 1573–1576 (1996).
3. Wdowiak, T. J. *et al.* Presence of an iron-rich nanophase material in the upper layer of the Cretaceous-Tertiary boundary clay. *Meteorit. Planet. Sci.* **36,** 123–133 (2001).
4. Dansgaard, W. *et al.* Evidence for general instability of past climate from a 250-kyr ice core record. *Nature* **364,** 218–220 (1993).
5. Hunten, D. M., Turco, R. P. & Toon, O. B. Smoke and dust particles of meteoric origin in the mesosphere and stratosphere. *J. Atmos. Sci.* **37,** 1342–1357 (1980).
6. Love, S. G. & Brownlee, D. E. Heating and thermal transformation of micrometeoroids entering the Earth's atmosphere. *Icarus* **89,** 26–43 (1991).
7. Prather, M. J. & Rodriguez, J. M. Antarctic ozone: meteoric control of HNO_3. *Geophys. Res. Lett.* **15,** 1–4 (1988).
8. Johnsen, S. J. *et al.* Oxygen isotope and palaeotemperature records from six Greenland ice-core stations: Camp Century, Dye-3, GRIP, GISP2, Renland and NorthGRIP. *Quat. Sci.* **16,** 299–307 (2001).
9. Wedepohl, K. H. The composition of the continental crust. *Geochim. Cosmochim. Acta* **59,** 1217–1232 (1995).
10. Hong, S., Candelone, J. P. & Boutron, C. F. Changes in zinc and cadmium concentrations in Greenland ice during the past 7760 years. *Atmos. Environ.* **31,** 2235–2242 (1997).
11. Zoller, W. H., Parrington, J. R. & Kotra, J. M. P. Iridium enrichment in airborne particles from Kilauea Volcano: January 1983. *Science* **222,** 1118–1121 (1983).
12. Anders, E. & Grevesse, N. Abundances of the elements: Meteoritic and solar. *Geochim. Cosmochim. Acta* **53,** 197–214 (1989).
13. Karner, D. B. *et al.* Extraterrestrial accretion from the GISP2 ice core. *Geochim. Cosmochim. Acta* **67,** 751–763 (2003).
14. Gabrielli, P. *et al.* Determination of Ir and Pt down to the sub-femtogram per gram level in polar ice by ICP-SFMS using preconcentration and a desolvation system. *J. Anal. At. Spectrom.* **19,** 831–837 (2004).
15. Love, S. G. & Brownlee, D. E. A direct measurement of the terrestrial mass accretion rate of cosmic dust. *Science* **262,** 550–553 (1993).
16. Plane, J. M. C. A new time-resolved model of the mesospheric Na layer: constraints on the meteor input function. *Atmos. Chem. Phys. Discuss.* **4,** 39–69 (2004).
17. Mathews, J. D., Janches, D., Meisel, D. D. & Zhou, Q. H. The micrometeoroid mass flux into the upper atmosphere: Arecibo results and a comparison with prior estimates. *Geophys. Res. Lett.* **28,** 1929–1932 (2001).
18. Manson, A. H. *et al.* Comparison between reference atmosphere winds and radar winds from selected locations. *Adv. Space Res.* **10,** 233–243 (1990).
19. Hughes, D. W. in *Cosmic Dust* (ed. McDonnel, J. A. M.) 123–185 (Wiley, London, 1978).
20. Ravizza, G. & Pyle, D. PGE and Os isotopic analysis of single sample aliquots with NiS fire assay preconcentration. *Chem. Geol.* **141,** 251–268 (1997).
21. Svensson, A., Biscaye, P. E. & Grousset, F. E. Characterization of late glacial continental dust in the Greenland Ice Core Project ice core. *J. Geophys. Res.* **105,** 4637–4656 (2000).
22. Muller, R. A. & MacDonald, G. J. Glacial cycles and orbital inclination. *Nature* **377,** 107–108 (1995).
23. Boutron, C. F. & Patterson, C. C. Lead concentration changes in Antarctic ice during the Wisconsin/Holocene transition. *Nature* **323,** 222–225 (1986).
24. Hong, S. *et al.* Climate-related variations in lead concentrations and sources in Vostok Antarctic ice from 65,000 to 240,000 years BP. *Geophys. Res. Lett.* **30,** 2138–2142 (2003).
25. Peucker-Ehrenbrink, B. & Ravizza, G. The effects of sampling artifacts on cosmic dust flux estimates: A reevaluation of nonvolatile tracers (Os, Ir). *Geochim. Cosmochim. Acta* **64,** 1965–1970 (2000).
26. Taylor, S., Lever, J. H. & Harvey, R. Accretion rate of cosmic spherules measured at the South Pole. *Nature* **392,** 899–903 (1998).
27. Barbante, C. *et al.* Determination of Rh, Pd, and Pt in polar and alpine snow and ice by double-focusing ICPMS with microcentric nebulization. *Anal. Chem.* **71,** 4125–4133 (1999).
28. Brown, P., Spalding, R. E., ReVelle, D. O., Tagliaferri, E. & Worden, S. D. The flux of small near-Earth objects colliding with the Earth. *Nature* **420,** 294–296 (2002).
29. Maurette, M., Jehanno, C., Robin, E. & Hammer, C. U. Characteristics and mass distribution of extraterrestrial dust from the Greenland ice cap. *Nature* **328,** 699–702 (1987).
30. Jacobson, M. Z., Lu, R., Jensen, E. J. & Toon, O. B. Modelling coagulation among particles of different composition and size. *Atmos. Environ. A* **28,** 1327–1338 (1994).

Supplementary Information accompanies the paper on **www.nature.com/nature**.

Acknowledgements This work was supported in France by the Institut Universitaire de France, the Ministère de l'Environnement et de l'Amènagement du Territoire, the Agence de l'Environnement et de la Maîtrise de l'Energie, the Institut National des Sciences de l'Univers and the Université Joseph Fourier of Grenoble. In Italy, it was supported by the Antarctic National Research Programme, and in the UK, by the Natural Environment Research Council. We thank G. McFiggans for discussions regarding the aerosol growth model. This research was also supported by two Marie Curie fellowships of the European Community programme (IHP) and by the Alliance for Global Sustainability. This work is a contribution of GRIP organized by the European Science Foundation: we thank all the personnel working in the field in Greenland.

Competing interests statement The authors declare that they have no competing financial interests.

Correspondence and requests for materials should be addressed to C.B. (barbante@unive.it).

The impact of humidity above stratiform clouds on indirect aerosol climate forcing

Andrew S. Ackerman[1], Michael P. Kirkpatrick[2], David E. Stevens[3] & Owen B. Toon[4]

[1]*NASA Ames Research Center, Moffett Field, California 94035, USA*
[2]*University of Tasmania, Hobart, TAS 7001, Australia*
[3]*Lawrence Livermore National Laboratory, Livermore, California 94552, USA*
[4]*University of Colorado, Boulder, Colorado 80309, USA*

Some of the global warming from anthropogenic greenhouse gases is offset by increased reflection of solar radiation by clouds with smaller droplets that form in air polluted with aerosol particles that serve as cloud condensation nuclei[1]. The resulting cooling tendency, termed the indirect aerosol forcing, is thought to be comparable in magnitude to the forcing by anthropogenic CO_2, but it is difficult to estimate because the physical processes that determine global aerosol and cloud populations are poorly understood[2]. Smaller cloud droplets not only reflect sunlight more effectively, but also inhibit precipitation, which is expected

to result in increased cloud water[3,4]. Such an increase in cloud water would result in even more reflective clouds, further increasing the indirect forcing. Marine boundary-layer clouds polluted by aerosol particles, however, are not generally observed to hold more water[5–7]. Here we simulate stratocumulus clouds with a fluid dynamics model that includes detailed treatments of cloud microphysics and radiative transfer. Our simulations show that the response of cloud water to suppression of precipitation from increased droplet concentrations is determined by a competition between moistening from decreased surface precipitation and drying from increased entrainment of overlying air. Only when the overlying air is humid or droplet concentrations are very low does sufficient precipitation reach the surface to allow cloud water to increase with droplet concentrations. Otherwise, the response of cloud water to aerosol-induced suppression of precipitation is dominated by enhanced entrainment of overlying dry air. In this scenario, cloud water is reduced as droplet concentrations increase, which diminishes the indirect climate forcing.

Measuring the response of cloud water to changes in aerosol and droplet concentrations is extremely challenging because aerosol abundance typically covaries with meteorological conditions, entangling the microphysical and meteorological signals. For instance, when a regional-scale pollution plume flows offshore, cloud properties respond not only to the aerosol abundance but also to the dryness of the plume[8].

Ship tracks, which are plumes of enhanced albedo in clouds polluted by ship exhaust, provide a natural 'laboratory' for isolating the effects of aerosol changes on cloud properties. Results from simple theoretical models[3,4] suggest that cloud water should consistently increase in ship tracks, an expectation not generally confirmed by observations. The first reported airborne measurements of ship tracks[9] support the theoretical expectations, with cloud water nearly doubling as droplet concentrations (N) tripled from their background values of $\sim$30 cm^{-3}. Subsequent observations, however, tend to show just the opposite relationship, if any, with cloud water generally decreasing as droplet concentrations increase. For example, *in situ* measurements of over 60 ship-track interceptions during the Monterey Area Ship Tracks (MAST) field project off the coast of central California show that cloud water increases in some and decreases in others, with a slight decrease on average[5]. High-resolution, airborne remote-sensing of three ship tracks during MAST also show cloud water decreasing on average[6]. More recently, satellite observations of hundreds of ship tracks over the northeastern Pacific Ocean show a significant average decrease in cloud water[7].

Here we investigate the dependence of cloud water on droplet concentrations using model simulations based on stratocumulus measurements during three field projects: (1) a nocturnal case study of drizzling clouds over the northeastern Atlantic during the Atlantic Stratocumulus Transition Experiment (ASTEX)[10,11]; (2) a nocturnal study during the second Dynamics and Chemistry of Marine Stratocumulus project (DYCOMS-II) off the coast of southern California[12], with very light precipitation largely limited to the cloud deck[13]; and (3) an idealization of cloudy conditions measured over two days during the First ISCCP (International Satellite Cloud Climatology Project) Regional Experiment (FIRE-I), also off the coast of southern California. For each meteorological setting we ran a sequence of 8-h nocturnal model simulations (daytime simulations are discussed subsequently) in which only the aerosol concentration was varied. As seen in Fig. 1, only when the average precipitation rate at the surface exceeds $\sim$0.1 mm d^{-1} does the average liquid-water path (LWP) increase with droplet concentrations in the simulations. This drizzling regime is consistent with simple models[3,4] in which decreased drizzle allows LWP to increase. An increase of LWP with droplet concentrations is seen over the entire range of droplet concentrations realized for the ASTEX simulations ($\sim$25–350 cm^{-3}). For the DYCOMS-II and FIRE-I conditions LWP again increases with N, but only below droplet concentration thresholds of $\sim$35 and 225 cm^{-3}, respectively.

These increases in LWP with N occur despite an increase with N in the rate at which the boundary layer entrains dryer air from above. The entrainment rate always increases with N in our simulations (Fig. 1), consistent with theoretical arguments that precipitation dries out cloudy air in updrafts, which reduces the moisture available for evaporative cooling of downdrafts[14]. Precipitation thus decreases the kinetic energy available in the boundary layer to entrain warmer air from above the temperature inversion. Conversely, a reduction in precipitation accelerates entrainment.

The response of LWP to increasing droplet concentrations can be considered to be the result of a competition between the effects of precipitation at the surface and near cloud-top. Decreased precipitation at the surface tends to increase LWP, whereas decreased precipitation near cloud-top tends to increase entrainment and thus decrease LWP. Only when the surface precipitation is sufficiently strong can it dominate the LWP response.

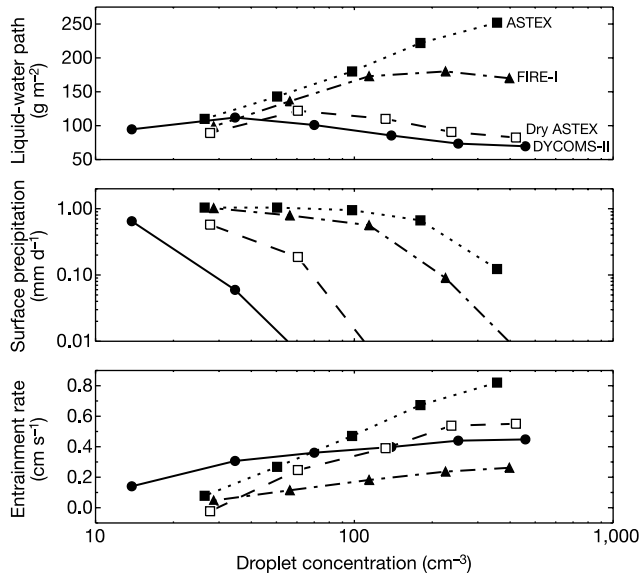

Figure 1 Liquid-water path and surface precipitation and entrainment rate as a function of cloud droplet number concentration. Liquid-water path and surface precipitation were averaged over the last two hours of 8-h simulations and the entrainment rate was averaged over eight hours. The cloud droplet number concentration was weighted by condensed water mass in each grid box. Curve labels correspond to meteorological conditions described in text. Entrainment rates ($\Delta z_i/\Delta t + Dz_i$, with z_i the horizontal average inversion height and D the large-scale horizontal wind divergence) are consistent with measured estimates of 0.38 $\pm$ 0.04 and 0.7 $\pm$ 0.3 cm s^{-1} for the DYCOMS-II and ASTEX cases[11,12] at droplet concentrations of $\sim$150 and 100 cm^{-3}.

Table 1 **Meteorological conditions used for stratocumulus simulations**

	ASTEX	FIRE-I	DYCOMS-II
Sea surface temperature (K)	290.4	289.0	292.5
Lifting condensation level (m)	340	250	620
Geostrophic wind speed (m s^{-1})	10	6	9
Inversion height (m)	700	600	840
Temperature increase across inversion (K)*	5.5	12	10
Moisture decrease across inversion (g kg^{-1})	1.0	3.0	7.5
Relative humidity above inversion (%)	70	40	10

*Difference in liquid-water potential temperature above and below the temperature inversion capping the boundary layer.

Precipitation depends on a number of environmental factors, and the three cases we consider here differ in a number of ways (see Table 1 and Methods). We find that the humidity of air overlying the boundary layer exerts a strong control on the surface precipitation rate. Moist air above the boundary layer is conducive to drizzle and thus favours the effect of precipitation at the surface: in the case of ASTEX the relative humidity above the boundary layer is ~70% and LWP monotonically increases with N over the range of droplet concentrations we consider (Fig. 1). In contrast, entrainment of dry air from above the boundary layer reduces cloud water and thereby suppresses drizzle, lowering the droplet concentration threshold above which changes in cloud water with N are dominated by the entrainment effect of precipitation. In the case of DYCOMS-II, with a relative humidity of ~10%, LWP decreases as N increases, except at extremely low droplet concentrations. In the intermediate case of FIRE-I, with a relative humidity close to 40%, LWP is seen to increase with N only at low-to-moderate droplet concentrations, and reverses at higher droplet concentrations.

To isolate the role of humidity above the boundary layer, we ran another sequence of simulations using the ASTEX meteorology, modified with warmer, dryer air above the boundary layer. In addition to decreasing the water vapour we also increased the temperature above the boundary layer to avoid stratocumulus break-up from cloud-top entrainment instability[15–17] (see Supplementary Fig. 1). The relative humidity above the boundary layer is ~25% in the modified conditions, substantially reducing precipitation and resulting in LWP decreasing as droplet concentrations increase beyond 60 cm^{-3} (Fig. 1). Thus we find that modifying the relative humidity above the boundary layer profoundly alters the balance between the competing effects of precipitation on LWP.

To clarify further the physics underlying the different responses of LWP to increasing droplet concentrations, we also ran simulations in which sedimentation of water is prevented. As seen in Fig. 2, drizzle reaches the surface for the ASTEX simulation (as observed), providing leverage for the effect of surface precipitation on LWP. Inhibiting precipitation results in moistening of the boundary layer and increasing LWP, as found in simpler models[3,4]. Suppressing drizzle does increase entrainment, but the entrained air is moist and does not dry the boundary layer effectively, and the cloud layer deepens as the cloud base sharpens.

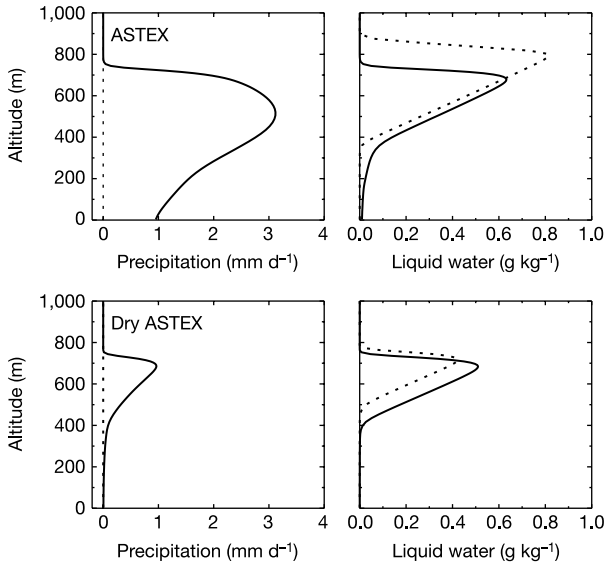

Figure 2 Horizontal average profiles of precipitation rate and liquid-water mixing ratio averaged over the last two hours of 8-h simulations. The top panels show simulations of baseline (observed) ASTEX conditions, and the bottom panels show simulations with humidity reduced above the boundary layer (see text). Dotted lines are for simulations without precipitation and solid lines for simulations with precipitation and droplet concentration of ~100 cm^{-3} as observed[11]. For the 'dry ASTEX' case, like the DYCOMS-II simulations and measurements[13] at comparable droplet concentrations, precipitation is dominated by sedimentation of cloud droplets rather than larger drops produced by collisions and coalescence.

For the ASTEX simulations with the same aerosol concentration but with the relative humidity reduced above the boundary layer, precipitation is drastically reduced by the entrainment of dry air. Because precipitation does not reach the surface for these conditions, it cannot be reduced further, and thus surface precipitation has no leverage on LWP. There is droplet sedimentation within the cloud layer, however; enough to restrict the entrainment rate. Completely suppressing sedimentation accelerates entrainment, drying the boundary layer and thinning the cloud layer as cloud base rises faster than cloud top.

We have also run simulations of daytime conditions, which show smaller trends in LWP as droplet concentrations increase; by offsetting longwave radiative cooling that drives stratocumulus convection, solar heating reduces convective mixing and results in a decreased response of LWP to microphysical changes (see Supplementary Table 1). In additional nocturnal simulations we find that diminished winds reduce the degree of turbulent mixing, which also results in a decreased response (Supplementary Table 1). Further simulations suggest that our results have effectively converged with respect to the grid spacing on the mesh we use (see Supplementary Fig. 2).

There are a number of implications of our findings. The response of cloud water to changes in droplet concentrations in our analysis suggests that the very concept of 'non-precipitating clouds' can be misleading. For cases in which little or no precipitation falls from a cloud layer, it is a mistake to assume that sedimentation of droplets within the cloud layer has no effect on entrainment and thus cloud water. On the contrary, it is the change in the precipitation flux from droplet sedimentation within such clouds that modulates the drying of the boundary layer by entrainment in our simulations.

Our results also show how cloud water can be depressed in clouds polluted by submicrometre aerosol particles acting as cloud nuclei, and the mechanism we describe here may well explain the decrease in LWP observed in high-resolution imagery of ship tracks[6]. (We recognize, however, that omitting partly cloudy and clear pixels may introduce a sampling bias that can lead to misleading conclusions[18].) Because of the difficulties in accurately retrieving surface precipitation rates below stratocumulus using satellite measurements, we recommend that satellite retrievals of cloud microphysics (not limited to overcast pixels) be combined with meteorological analyses to assess the dependence of LWP tendencies on humidity above the boundary layer.

In contrast to one-dimensional models that include drizzle but not cloud droplet sedimentation[3,4], our simulations show that LWP can decrease as droplet concentrations increase. Other models that treat cloud droplet sedimentation show that when convective mixing is suppressed by strong solar heating, LWP can decrease as N increases in stratocumulus with very light precipitation[19,20]. Those studies, however, were each limited to single meteorological settings, and did not address the role of humidity above the boundary layer. By considering a variety of meteorological settings, here we identify relative humidity above the boundary layer as a leading factor determining the response of cloud water to changes in droplet concentrations. When the air above the boundary layer is dry, we find that LWP decreases as N increases even in nocturnal simulations. Beyond marine stratocumulus, we recommend investigating the effect of overlying humidity on the response of cloud water to changes in droplet concentrations in other cloud types, such as continental and mixed-phase stratiform clouds, as well as in transitions between cloud regimes. Feedbacks with mesoscale and larger-scale circulations are also of interest.

Our findings indicate that global estimates from satellite observations of the indirect aerosol forcing in boundary-layer clouds[21] require the estimation not only of the regional changes in cloud droplet concentrations, but also of the covarying climatologies in relative humidity above stratocumulus regions. Also, predictions of climate change require global climate models to represent accurately not only such critical and challenging details as boundary-layer entrainment, but also its response to changes in cloud droplet sedimentation. Our results may help to explain why forward climate models, which consistently show an amplification of the 'Twomey effect'[22], tend to overestimate the overall indirect aerosol forcing compared to inverse calculations from simpler models constrained by the historical temperature record[23]. □

Methods

Model description

The fluid dynamics model is described in ref. 24. The computational domain extends 3.4 km in both horizontal directions and 1.5 km vertically (1 km for the FIRE-I simulations), with $64 \times 64 \times 86$ cells in the x, y and z directions respectively. Grid spacing is uniform horizontally and stretched vertically to give cells of height 6 m close to the surface and in the vicinity of the inversion. The model domain is translated with the geostrophic winds, thereby reducing numerical errors associated with advection. A sponge layer occupies the upper 250 m of the domain. Subgrid-scale fluxes are modelled using a dynamic turbulence model[25]. A modified version of the model in ref. 26 is used to treat surface-layer fluxes in the bottom 100 m of the domain. Subsidence and radiative forcings are linearly attenuated to zero in the 300 m above the inversion (defined as the average height where the total water mixing ratio exceeds a threshold that depends on the meteorological scenario) to prevent drift of the overlying atmospheric properties resulting from any unbalanced forcings. The cloud microphysics model is described in ref. 27 and the linkages with the fluid dynamics model are described elsewhere[28]. Particle size distributions are resolved into 20 bins over a range from 0.01 to 5 μm radius for dry condensation nuclei, which are assumed to consist of ammonium bisulphate, and over a range from 1 to 500 μm radius for activated cloud droplets. The total particle number concentration at each grid point is fixed in each simulation at 40, 75, 150, 300 and 600 cm^{-3} for the ASTEX and FIRE-I progressions, and additionally at 20 cm^{-3} for the DYCOMS-II sequence. The aerosol distributions are log-normal with a geometric mean radius of 0.1 μm and a geometric standard deviation of 1.5. Radiative transfer is calculated for each column once every minute with a two-stream model[29].

Set-up of model simulations

The ASTEX simulations are based on an idealization of the 12–13 June 1992 nocturnal stratocumulus measurements obtained by the UK Meteorological Research Flight C-130 aircraft (flight A209) of the Atlantic Stratocumulus Transition Experiment[10,11], with model initialization and forcings adapted from the Fourth Global Energy and Water Experiment (GEWEX) Cloud System Studies (GCSS) Boundary Layer Cloud Workshop[30]. We depart from the workshop specifications by initializing our model domain as initially cloud-free and using surface similarity for surface fluxes, with the sea surface temperature fixed at 292.4 K. As done in the Eighth GCSS Boundary Layer Cloud Workshop[31] the fluxes of heat and moisture are fixed during the first two hours, in this case at 10 and 30 $W m^{-2}$, respectively. Instead of the radiative flux parameterization in the workshop specification we use a two-stream radiative transfer model in which the precipitable water vapour overlying the model domain is fixed at 2.2 cm, resulting in a net (upward) longwave flux of 70 $W m^{-2}$ above the boundary layer after the cloud layer forms. For the 'dry ASTEX' simulations the surface moisture flux during the first two hours is increased to 60 $W m^{-2}$ and the overlying precipitable water vapour is increased to 3.2 cm. The inversion height is defined as the average altitude where the total water mixing ratio (in grams of water per kilogram of dry air) is 8 $g kg^{-1}$.

The DYCOMS-II simulations are based on an idealization of nocturnal stratocumulus observations obtained during the first research flight of the second Dynamics and Chemistry of Marine Stratocumulus field study[13], with model initialization and forcings adapted from step 4 of the Eighth GCSS Boundary Layer Cloud Workshop[31]. The precipitable water vapour overlying the model domain is fixed at 1.85 cm, resulting in a net longwave flux of 80 $W m^{-2}$ above the boundary layer after the cloud layer forms. The total water mixing ratio defining the inversion height is 8 $g kg^{-1}$.

The FIRE-I simulations are based on an idealization of stratocumulus observations obtained during 14–15 July 1987 of the First ISCCP Regional Experiment with model initialization and forcings adapted from the European Project on Cloud Systems in Climate Models (EUROCS) stratocumulus case[32]. We use a large-scale divergence rate of 5×10^{-6} s^{-1} and as in other cases ignore any large-scale advective forcings. The fluxes of heat and moisture during the first two hours are fixed at 5 and 24 $W m^{-2}$, respectively. The precipitable water vapour overlying the model domain is fixed at 2 cm, resulting in a net longwave flux of 75 $W m^{-2}$ above the boundary layer after the cloud layer forms. The total water mixing ratio defining the inversion height is 9 $g kg^{-1}$.

Received 26 May; accepted 21 October 2004; doi:10.1038/nature03174.

1. Twomey, S. Pollution and the planetary albedo. *Atmos. Environ.* **8,** 1251–1256 (1974).
2. Houghton, J. T. *et al.* (eds) *Climate Change 2001: The Scientific Basis. Contribution of Working Group I to the Third Assessment Report of the Intergovernmental Panel on Climate Change* Ch. 5 and 6 (Cambridge Univ. Press, UK/USA, 2001).
3. Albrecht, B. Aerosols, cloud microphysics, and fractional cloudiness. *Science* **245,** 1227–1230 (1989).
4. Pincus, R. & Baker, M. B. Effect of precipitation on the albedo susceptibility of clouds in the marine boundary layer. *Nature* **372,** 250–252 (1994).
5. Ackerman, A. S. *et al.* Effects of aerosols on cloud albedo: Evaluation of Twomey's parameterization of cloud susceptibility using measurements of ship tracks. *J. Atmos. Sci.* **57,** 2684–2695 (2000).
6. Platnick, S. *et al.* The role of background cloud microphysics in the radiative formation of ship tracks. *J. Atmos. Sci.* **57,** 2607–2624 (2000).
7. Coakley, J. A. Jr & Walsh, C. D. Limits to the aerosol indirect radiative effect derived from observations of ship tracks. *J. Atmos. Sci.* **59,** 668–680 (2002).
8. Brenguier, J. L. *et al.* Radiative properties of boundary layer clouds: Droplet effective radius versus number concentration. *J. Atmos. Sci.* **57,** 803–821 (2000).
9. Radke, L. F., Coakley, J. A. J. Jr & King, M. D. Direct and remote sensing observations of the effects of ships on clouds. *Science* **246,** 1146–1149 (1989).
10. Duynkerke, P. G., Zhang, H. & Jonker, P. J. Microphysical and turbulent structure of nocturnal stratocumulus as observed during ASTEX. *J. Atmos. Sci.* **52,** 2763–2777 (1995).
11. Bretherton, C. S., Austin, P. & Siems, S. T. Cloudiness and marine boundary layer dynamics in the ASTEX Lagrangian experiments: Part II: Cloudiness, drizzle, surface fluxes, and entrainment. *J. Atmos. Sci.* **52,** 2724–2735 (1995).
12. Stevens, B. *et al.* On entrainment rates in nocturnal marine stratocumulus. *Q. J.R. Meteorol. Soc.* **129,** 3469–3493 (2003).
13. Stevens, B. *et al.* Dynamics and chemistry of marine stratocumulus—DYCOMS-II. *Bull. Am. Meteorol. Soc.* **84,** 579–593 (2003).
14. Stevens, B., Cotton, W. R., Feingold, G. & Moeng, C.-H. Large-eddy simulations of strongly precipitating, shallow, stratocumulus-topped boundary layers. *J. Atmos. Sci.* **55,** 3616–3638 (1998).
15. Randall, D. A. Conditional instability of the first kind upside-down. *J. Atmos. Sci.* **37,** 125–130 (1980).
16. Deardorff, J. W. Cloud top entrainment instability. *J. Atmos. Sci.* **37,** 131–147 (1980).
17. MacVean, M. K. & Mason, P. J. Cloud-top entrainment instability through small-scale mixing and its parameterization in numerical models. *J. Atmos. Sci.* **47,** 1012–1030 (1990).
18. Ackerman, A. S., Toon, O. B., Stevens, D. E. & Coakley, J. A. Jr. Enhancement of cloud cover and suppression of noctural drizzle in stratocumulus polluted by haze. *Geophys. Res. Lett.* **30,** doi:10.1029/2002GL016634 (2003).
19. Ackerman, A. S., Toon, O. B. & Hobbs, P. V. Numerical modeling of ship tracks produced by injections of cloud condensation nuclei into marine stratiform clouds. *J. Geophys. Res.* **100,** 7121–7133 (1995).
20. Jiang, H., Feingold, G. & Cotton, W. R. Simulations of aerosol-cloud-dynamical feedbacks resulting from entrainment of aerosol into the marine boundary layer during the Atlantic Stratocumulus Transition Experiment. *J. Geophys. Res.* **107,** doi:10.1029/2001JD001502 (2002).
21. Nakajima, T., Higurashi, A., Kawamoto, K. & Penner, J. E. A possible correlation between satellite-derived cloud and aerosol microphysical parameters. *Geophys. Res. Lett.* **28,** 1171–1174 (2001).
22. Haywood, J. & Boucher, O. Estimates of the direct and indirect radiative forcing due to tropospheric aerosols: A review. *Rev. Geophys.* **38,** 513–543 (2000).
23. Knutti, R., Stocker, T. F., Joos, F. & Plattner, G.-K. Constraints on radiative forcing and future climate change from observations and climate model ensembles. *Nature* **416,** 719–723 (2002).
24. Stevens, D. E., Ackerman, A. S. & Bretherton, C. S. Effect of domain size and numerical resolution on the simulation of shallow cumulus convection. *J. Atmos. Sci.* **59,** 3285–3301 (2002).
25. Germano, M., Piomelli, U., Moin, P. & Cabot, W. H. A dynamic subgrid-scale eddy viscosity model. *Phys. Fluids A* **3,** 1760–1765 (1991).
26. Brown, A. R., Hobson, J. M. & Wood, N. Large-eddy simulation of neutral turbulent flow over rough sinusoidal ridges. *Boundary-Layer Meteorol.* **98,** 411–441 (2001).
27. Ackerman, A. S., Toon, O. B. & Hobbs, P. V. A model for particle microphysics, turbulent mixing, and radiative transfer in the stratocumulus-topped marine boundary layer and comparisons with measurements. *J. Atmos. Sci.* **52,** 1204–1236 (1995).
28. McFarlane, S., Evans, F. & Ackerman, A. S. A Bayesian algorithm for the retrieval of liquid water cloud properties from microwave radiometer and millimeter radar data. *J. Geophys. Res.* **107,** doi:10.1029/2001JD001011 (2002).
29. Toon, O. B., McKay, C. P., Ackerman, T. P. & Santhaman, K. Rapid calculation of radiative heating and photodissociation rates in inhomogeneous multiple scattering atmospheres. *J. Geophys. Res.* **94,** 16287–16301 (1989).
30. Fourth Global Energy and Water Experiment (GEWEX) Cloud System Studies (GCSS) Boundary Layer Cloud Workshop ⟨http://www.phys.uu.nl/~wwwimau/old/ASTEX/astexcomp.html⟩ (12–16 August 1996, Clermont-Ferrand, France).
31. Stevens, B. *et al.* Evaluation of large-eddy simulations via observations of nocturnal marine stratocumulus. *Mon. Weath. Rev.* (in the press); Eighth GCSS Boundary Layer Cloud Workshop ⟨http://www.atmos.ucla.edu/~bstevens/dycoms/dycoms.html⟩ (29–31 October 2003, Broomfield, Colorado, USA).
32. Duynkerke, P. G. *et al.* Observations and numerical simulations of the diurnal cycle of the EUROCS stratocumulus case. *Q. J.R. Meteorol. Soc.* (in the press); European Project on Cloud Systems in Climate Models ⟨http://www.phys.uu.nl/~wwwimau/research/atm_dyn/EUROCS_PART_I/eurocs.html⟩ (16–19 December 2002, Madrid, Spain).

Supplementary Information accompanies the paper on **www.nature.com/nature**.

Acknowledgements We thank A. Fridlind and E. Jensen for comments on the manuscript, N. Mansour, J. Ferziger, and R. Street for discussions regarding the subgrid-scale model, and B. Stevens for providing the DYCOMS-II measurements to the Eighth GCSS Boundary Layer Cloud Workshop. This work was supported by the Radiation Science Program of NASA.

Competing interests statement The authors declare that they have no competing financial interests.

Correspondence and requests for material should be addressed to A.S.A. (andrew.ackerman@nasa.gov).

Supplementary Table 1. Relative change of liquid water path (LWP) with respect to cloud droplet concentration (N) between averages over the last two hours of 8-h simulations with aerosol concentrations of 150 and 300 cm^{-3}. For cases with solar radiation, sun angles are computed for summer solstice at the latitude of the ASTEX measurements (38°), and time zero corresponds to 8 AM local solar time. The minimum, median, and maximum for the DYCOMS-II conditions are computed from an ensemble of six simulations comprised of three simulations at each aerosol concentration, in which the initial perturbations of temperature and water vapor were varied by giving a different seed to the pseudo-random number generator.

Simulations	$\Delta \ln \mathrm{LWP} / \Delta \ln N$
ASTEX baseline	0.34
ASTEX with solar radiation	0.31
dry ASTEX	-0.33
dry ASTEX with solar radiation	-0.27
FIRE-I baseline	0.06
DYCOMS-II baseline minimum	-0.35
DYCOMS-II baseline median	-0.27
DYCOMS-II baseline maximum	-0.22
DYCOMS-II low shear*	-0.22

*Geostrophic wind speed reduced to 5 m s^{-1}, minimum measured during DYCOMS-II project.

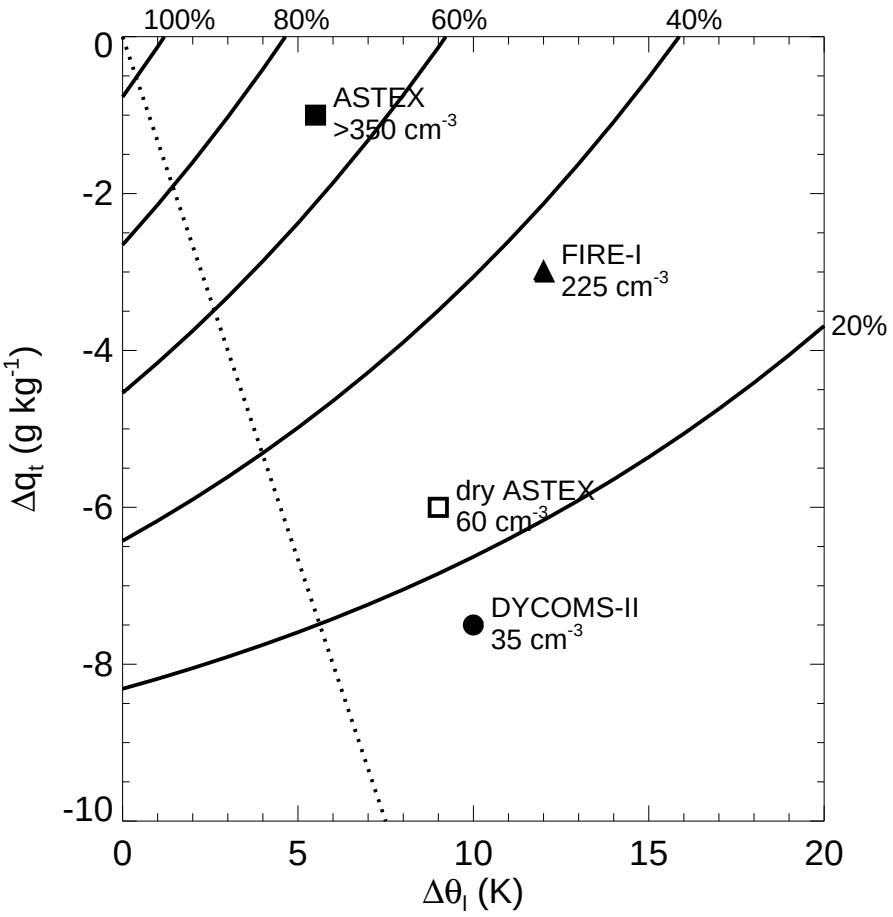

Supplementary Figure 1. Differences between the boundary layer and overlying air of total water (vapor + liquid) mixing ratio (Δq_t) and liquid water potential temperature ($\Delta\theta_l$) for the conditions used in our stratocumulus simulations (Δ = value in the overlying air minus the value in the boundary layer). The points are labeled with the threshold droplet number concentration (N) above which LWP decreases as N increases in the simulations (see Figure 1). The cloud-top entrainment instability of MacVean and Mason (1990) is shown as a dotted line; persistent stratocumulus are only expected to the right of this line. Stratocumulus breakup is expected when the evaporative cooling that occurs during energetically favorable mixing of clear and cloudy air results in mixed air that is less dense than unmixed cloudy air. The solid curves are contours of relative humidity above the boundary layer (the baseline ASTEX conditions are used for these relative humidity contours, which weakly depend on cloud-top thermodynamic conditions).

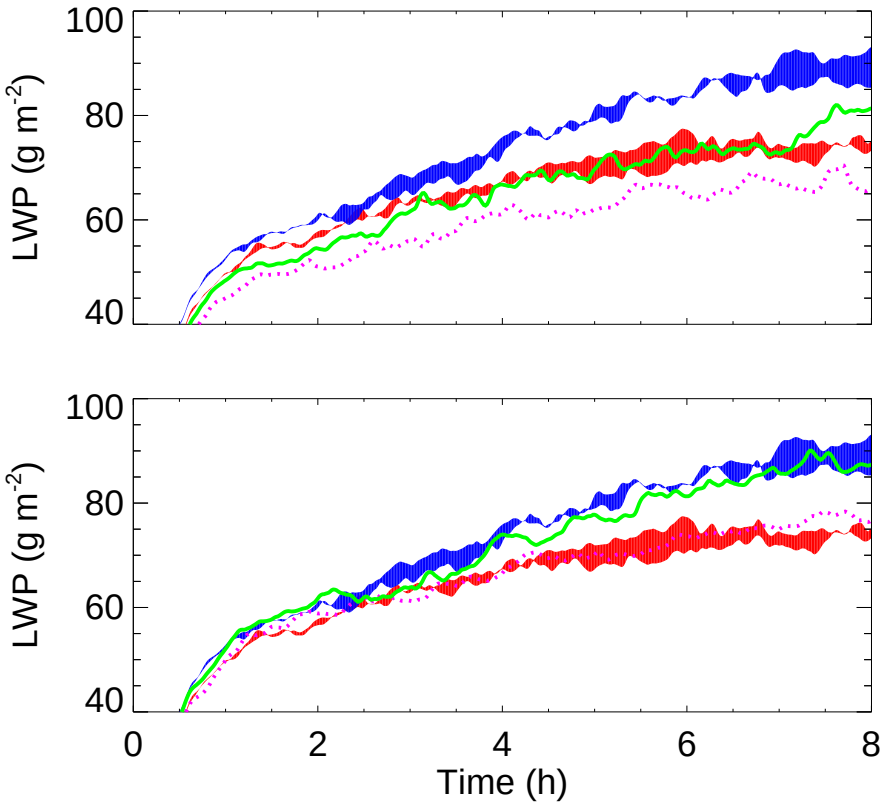

Supplementary Figure 2. Evolution of domain average liquid water path (LWP) for DYCOMS-II simulations using different grid meshes. Blue and red shaded areas are envelopes of ensembles (three simulations at each aerosol concentration, using different initial pseudo-random perturbations of temperature and vapor) on a 64x64x86 grid with aerosol concentrations of 150 and 300 cm^{-3}, respectively. Solid green and dotted magenta lines in top (bottom) panel are simulations on 48x48x64 (96x96x128) grid with aerosol concentrations of 150 and 300 cm^{-3}, respectively. Beyond the comparable decrease of LWP seen in all the simulations as aerosol concentrations increase, the absolute values of LWP agree on the two finest grids, suggesting that the results have converged with respect to grid spacing on the 64x64x86 mesh that is used in all the other simulations reported in this study.